

1 **AnisoVeg: Anisotropy and Nadir-normalized MODIS MAIAC datasets for satellite
2 vegetation studies in South America**

3 Ricardo Dalagnol^{1,2,3,*}, Lênio Soares Galvão³, Fabien Hubert Wagner^{1,2}, Yhasmin Mendes
4 Moura^{4,5}, Nathan Gonçalves⁶, Yujie Wang^{7,8}, Alexei Lyapustin⁷, Yan Yang¹, Sassan Saatchi^{1,2},
5 Luiz Eduardo Oliveira Cruz Aragão^{3,9}

6 1 Center for Tropical Research, Institute of the Environment and Sustainability, University of
7 California, Los Angeles, Los Angeles, CA 90095, USA.

8 2 NASA-Jet Propulsion Laboratory, California Institute of Technology, Pasadena, CA 91109,
9 USA.

10 3 Earth Observation and Geoinformatics Division, National Institute for Space Research-INPE,
11 São José dos Campos, SP, 12227-010, Brazil.

12 4 Institute of Geography and Geoecology, Karlsruhe Institute of Technology, Karlsruhe,
13 Germany.

14 5 Centre for Landscape and Climate Research, School of Geography, Geology, and the
15 Environment, University of Leicester, Leicester, UK.

16 6 Michigan State University, Department of Forestry, College of Agriculture & Natural
17 Resources, East Lansing, MI, USA.

18 7 NASA Goddard Space Flight Center, Greenbelt, MD, United States.

19 8 Joint Center for Earth Systems Technology, University of Maryland Baltimore County, 1000
20 Hilltop Circle, Baltimore, MD.

21 9 Geography, College of Life and Environmental Sciences, University of Exeter, Exeter EX44RJ,
22 UK.

23

24 * Corresponding author. E-mail: ricds@hotmail.com.

25

26 **This document includes:** main manuscript, figures and tables.

27 **Abstract**

28 The AnisoVeg product consists of monthly 1-km composites of anisotropy (ANI) and nadir-
29 normalized (NAD) surface reflectance layers obtained from the Moderate Resolution Imaging
30 Spectroradiometer (MODIS) sensor over the entire South America. The satellite data were pre-
31 processed using the Multi-Angle Implementation Atmospheric Correction (MAIAC). The
32 AnisoVeg product spans 22 years of observations (2000 to 2021) and includes the reflectance of
33 MODIS bands 1 to 8 and two vegetation indices (VIs): Normalized Difference Vegetation Index
34 (NDVI) and Enhanced Vegetation Index (EVI). While the NAD layers reduce the data variability
35 added by bidirectional effects on the reflectance and VI time series, the unique ANI layers allow
36 the use of this multi-angular data variability as a source of information for vegetation studies. The
37 AnisoVeg product has been generated using daily MODIS MAIAC data from both Terra and
38 Aqua satellites, normalized for a fixed solar zenith angle ($SZA = 45^\circ$), modelled for three sensor
39 view directions (nadir, forward, and backward scattering), and aggregated to monthly composites.
40 The anisotropy was calculated by the subtraction of modelled backward and forward scattering
41 surface reflectance. The release of the ANI data for open usage is novel, as well as the NAD data
42 at an advance processing level. We demonstrate the use of such data for vegetation studies using
43 three types of forests in eastern Amazon with distinct gradients of vegetation structure and
44 aboveground biomass (AGB). The gradient of AGB was positively associated with ANI, while
45 NAD values were related to different canopy structural characteristics. This was further illustrated
46 by the strong and significant relationship between EVI_{ANI} and forest height observations from the
47 Global Ecosystem Dynamics Investigation (GEDI) LiDAR sensor considering a simple linear
48 model ($R^2 = 0.55$). Overall, the time series of the AnisoVeg product (NAD and ANI) provide
49 distinct information for various applications aiming at understanding vegetation structure,
50 dynamics, and disturbance patterns. All data, processing codes and results are made publicly
51 available to enable research and the extension of AnisoVeg products for other regions outside the
52 South America. The code can be found at <https://doi.org/10.5281/zenodo.6561351> (Dalagnol and
53 Wagner, 2022), EVI_{ANI} and EVI_{NAD} can be found as assets in the Google Earth Engine (GEE)
54 (described in the data availability section), and the full dataset is available at the open repository
55 <<https://doi.org/10.5281/zenodo.3878879>> (Dalagnol et al., 2022).

56 **Key-words:** AnisoVeg, South America, vegetation structure, forest monitoring, MODIS.

57

58 **1. Introduction**

59 The anisotropy is defined as the departure from Lambertian scattering (isotropic), caused by the
60 physical structure of media through which photons pass. Because most land covers are not
61 Lambertian (isotropic), the surface reflectance measured by satellite sensors varies with the view
62 zenith angle (VZA), view direction (backward or forward scattering), and solar zenith angle
63 (SZA) (Galvão et al., 2011). This is especially valid for images acquired over vegetated surfaces
64 by large field-of-view (FOV) instruments such as the Moderate Resolution Imaging
65 Spectroradiometer (MODIS) (Bhandari et al., 2011). MODIS has a wide swath scanning $\pm 55^\circ$
66 from nadir on board the Terra and Aqua satellites. For example, a reflected signal coming from
67 the backward scattering direction of MODIS under a large VZA and close-to-zero relative
68 azimuth angle (RAA) between the satellite and sun (sun behind the platform) is generally higher
69 than that coming from the nadir ($VZA = 0^\circ$) or forward scattering direction (platform facing the
70 sun at $RAA = 180^\circ$). Moreover, the SZA also varies seasonally and across geographical locations,
71 affecting the amounts of shadows in the surfaces observed by satellites (Galvão et al., 2013). Such
72 view-illumination effects are dependent on the land cover types and their magnitude relates to
73 differences in biophysical properties of the vegetation (Galvão et al., 2004; Sims et al., 2011).
74 Therefore, the vegetation anisotropy can be seen antagonistically as sources of noise and

75 biophysical information in the time-series analysis of vegetation indices (VIs) calculated from
76 MODIS. As a source of noise, one may consider that the reflected signal toward the large FOV
77 satellite sensors varies with distinct view-illumination geometries of data acquisition over the
78 same surface. As a source of information, one may highlight that the anisotropy is land-cover type
79 dependent, showing spectral variations that may be associated, for instance, with changes in
80 vegetation structure across different forests.

81 To reduce the bidirectional effects as a source of noise, a nadir-normalized dataset can be created.
82 We can normalize the surface reflectance of the MODIS bands to a specific set of VZA and SZA
83 using the bidirectional reflectance distribution function (BRDF), represented by a model such as
84 the Ross-Thick Li-Sparse (RTLS) (Wanner et al., 1995). To ensure confidence in the data
85 analysis, we can also use the Multi-Angle Implementation Atmospheric Correction (MAIAC) for
86 atmospheric correction. MAIAC is a new generation of cloud screening and atmospheric
87 correction algorithm that uses an adaptive time series analysis and processing of groups of pixels
88 to derive atmospheric aerosol concentration, cloud mask and surface reflectance without typical
89 empirical assumptions (Lyapustin et al., 2011, 2012). By mitigating atmospheric interference and
90 advancing the accuracy of surface reflectance over tropical vegetation by a factor of 3 to 10,
91 MAIAC offers substantial improvement over conventional products such as the MOD09 (Hilker
92 et al., 2012). Because of the better data quality retrieval, MAIAC is also an alternative to the
93 MCD43A4 16-day Nadir Bidirectional Reflectance Distribution Function (BRDF)-Adjusted
94 Reflectance (NBAR) product due to the less variable seasonal signal (3 to 10 times) over
95 evergreen forests resultant from reduced effects of sun-view geometry. While the MCD43A4
96 NBAR product offers view-illumination correction, using the MAIAC products one can also
97 correct for solar illumination effects at the same time. Due to the improvements in cloud detection,
98 aerosol retrieval and atmospheric correction, the MAIAC algorithm provides from 4 to 25% more
99 high-quality retrievals than the traditional MOD09 product, with the largest estimate being
100 observed for tropical regions (Lyapustin et al., 2021). Studies have used MODIS MAIAC
101 observations with nadir-normalized geometry to assess Amazonian forests' structure, functioning,
102 and impacts of environmental and climate change (Hilker et al., 2014; Wagner et al., 2017;
103 Anderson et al., 2018; Dalagnol et al., 2018; Fonseca et al., 2019; Bontempo et al., 2020;
104 Gonçalves et al., 2020; Zhang et al., 2021). For instance, such products provided reliable time
105 series of surface reflectance data that allowed to identify large-scale communities of bamboo
106 species and their dynamics in the southwest Amazon (Dalagnol et al., 2018). Lastly, by improving
107 the cloud screening and minimizing BRDF artifacts in comparison to uncorrected data, the
108 MAIAC greatly contributed to the understanding of the long-standing debate in the Amazon over
109 the possible existence of the green-up phenomenon observed during the dry season of each year
110 or with severe droughts (Morton et al., 2014; Bi et al., 2015; Saleska et al., 2016; Wu et al., 2017).
111 The existence of this phenomenon has implications on the comprehension of the resilience of
112 tropical forests to climate change.

113 To use the bidirectional effects as a source of information, we generate an anisotropy dataset that
114 is dependent on land-cover types and captures the variations of sunlit and shaded canopy
115 components viewed by the sensors (Chen et al., 2003; Gao, 2003). The use of multi-angular
116 information to obtain metrics of anisotropy and extract information on forest structure was
117 suggested two decades ago (Gobron et al., 2002; Diner et al., 2005). One of the early experiments
118 exploring the use of anisotropy to extract information about vegetation structure were conducted
119 by calculating the ratio between backward and forward scattering data and generating the
120 anisotropy index (ANIX) on studying short-stature grass-type vegetation (Sandmeier et al., 1998).
121 Other indices have been developed and validated afterwards (Schaaf et al., 2002; Lacaze et al.,
122 2002; Chen et al., 2005; Pocewicz et al., 2007; Moura et al., 2015; Sharma et al., 2021). However,
123 this remains an understudied topic with limited results reported in the literature, especially in
124 tropical regions. For instance, observations from the Multi-angle Imaging Spectroradiometer

(MISR)/Terra in the backward and forward scattering directions facilitated the discrimination of savanna physiognomies in Brazil (Liesenber et al., 2007). MODIS MAIAC data from both directions were also used to calculate an anisotropic VI that explained part of the large-scale photosynthetic activity in the Amazon, where higher photosynthetic activity was associated to higher anisotropy values (Sousa et al., 2017). Moura et al. (2015) employed a more sophisticated approach based on scattering at backward and forward view directions using multi-temporal and multi-angular observations of MAIAC MODIS and BRDF modelling. The resultant metrics of anisotropy were further validated against field and airborne Light Detection And Ranging (LiDAR) observations, showing strong linear relationship with leaf area index (LAI) ($R^2 = 0.70$ - 0.88), canopy heterogeneity ($R^2 = 0.54$), and photosynthetic activity ($R^2 = 0.73$ - 0.98) (Moura et al., 2015; Moura et al., 2016; Hilker et al., 2017). Although showing great potential in vegetation studies, the aforementioned anisotropy metrics were never computed over larger areas of the world such as proposed in this study for South America.

The objective of this work is to present the AnisoVeg product, and how it can be used for vegetation studies. We use MODIS Collection 6 (C6) MAIAC (Lyapustin et al., 2018) monthly data (2000-2021) generated at 1-km spatial resolution for the entire South America with two different types of layers: (1) nadir-normalized (NAD) data for the surface reflectance of MODIS bands 1 to 8 and two VIs (NDVI and EVI); and (2) anisotropy data (ANI) calculated from the difference between backward and forwarding scattering estimates of bands 1 to 8 and VIs (Moura et al., 2015). The motivations for generating this product extend from developing applications of multi-angle observations for vegetation studies to producing analysis-ready and openly available datasets of anisotropy and nadir metrics for a larger community of users. The paper is organized in several sections to present the processing steps for generating the AnisoVeg products, a brief evaluation of data products over experimental areas, and finally an example of its potential application in vegetation studies.

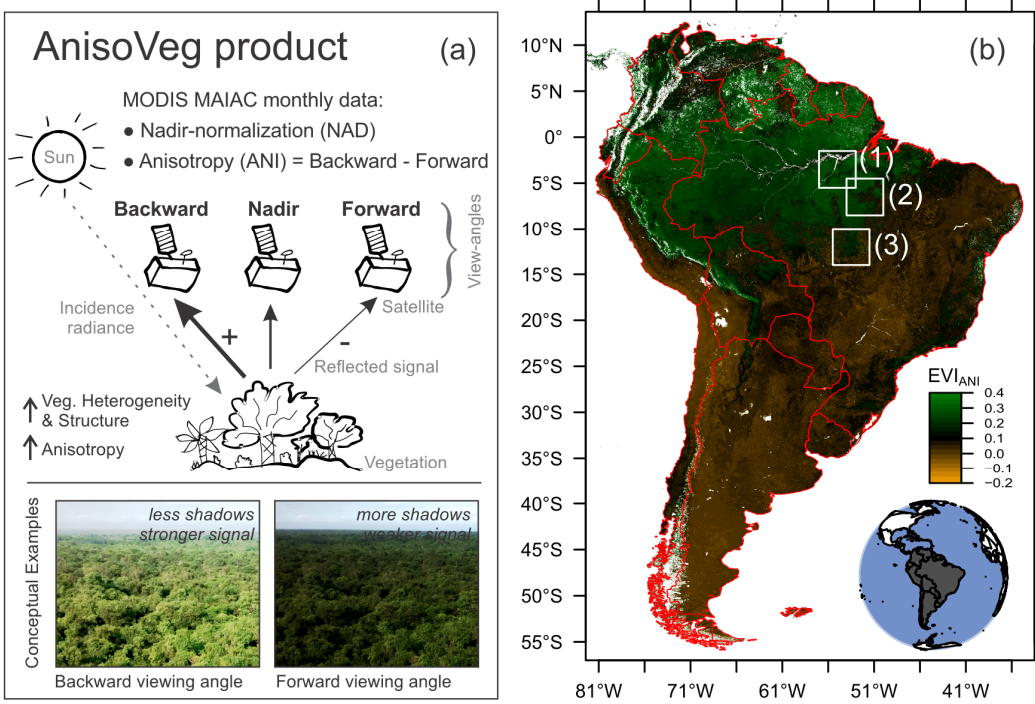
150

151 **2. Methodology to compute the AnisoVeg product**

152 **2.1. Daily MODIS MAIAC surface reflectance data over South America**

153 Daily surface reflectance data were obtained from the MODIS product MCD19A1 v006
154 (collection 6) for the tiles covering South America (Figure 1). According to the MODIS traditional
155 tiling system, these tiles ranged from 9-14 (horizontal) and 7-14 (vertical). The input data
156 consisted in cross-calibrated surface reflectance from Terra and Aqua satellites on eight spectral
157 bands (Table 1) with 1-km spatial resolution from 2000 to 2021 (Lyapustin & Wang, 2018;
158 <http://dx.doi.org/10.5067/MODIS/MCD19A1.006>). This product provides surface reflectance
159 data corrected for atmospheric effects by the MAIAC algorithm, and controlled for cloud-free
160 and clear-to-moderately turbid conditions with Aerosol Optical Depth (AOD) at 0.47 μ m below
161 1.5 (Lyapustin et al., 2018). The MAIAC algorithm uses a time series approach for improved
162 cloud filtering amongst other filters such as surface reflectance change in order to provide the
163 most accurate surface reflectance estimates. The raw data were obtained from the NASA's Level-
164 1 and Atmosphere Archive and Distribution System (LAADS) Distributed Active Archive Center
165 (DAAC) available at <https://ladsweb.modaps.eosdis.nasa.gov/archive/allData/6/MCD19A1/>.

166



167

168 Figure 1 – AnisoVeg product concept and the area of coverage. (a) Schematic representation
 169 showing the observational geometry and the processing steps for producing NAD and ANI data
 170 from MODIS and to provide information on vegetation heterogeneity and structure, and (b) the
 171 visualization of the anisotropy EVI (EVI_{ANI}) for South America from August 2021 at 1-km spatial
 172 resolution, showing the coverage of the product in South America and the location of three sites
 173 used to demonstrate potential applications. The sites are: (1) Tapajós National Forest, (2) São
 174 Felix do Xingu, and (3) Xingu Park. Red lines indicate the countries boundaries.

175

176 Table 1 – MODIS spectral bands. NIR = near infrared; SWIR = shortwave infrared.

Band number	Band name	Wavelength (nm)
1	Red	620–670
2	NIR-1	841–876
3	Blue-1	459–479
4	Green	545–565
5	NIR-2	1230–1250
6	SWIR-1	1628–1652
7	SWIR-2	2105–2155
8	Blue-2	405–420

177

178 2.2. The AnisoVeg product

179 The AnisoVeg product consists of two main types of data spanning from 2000 to 2021 in monthly
 180 composites at 1-km spatial resolution: (a) the nadir-normalized (NAD) data; and (b) the
 181 anisotropy (ANI) data. Each data type has 10 layers corresponding to the MODIS bands 1 to 8,
 182 and two VIs (NDVI and EVI). Additionally, the product provides auxiliary layers of backward
 183 scattering and forward scattering, including part of the bands (description on section 5).

184

185 **2.2.1. The nadir-normalized (NAD) data**

186 In order to minimize the differences in sun-sensor geometry between the MODIS scenes and
 187 generate the NAD dataset, the daily surface reflectance data were normalized to a fixed 45° SZA
 188 and to nadir observation (VZA = 0°) using the BRDF and the Ross-Thick Li-Sparse (RTLS) model
 189 (Wanner et al., 1995). Parameters of the RTLS BRDF model are part of the MAIAC product suite
 190 (MCD19A3 product) reported every 8 days. The MAIAC algorithm detects significant land cover
 191 changes (e.g. fire, deforestation) within the 8-day period and does not use those observations for
 192 the BRDF inversion (Lyapustin et al., 2018). A minimum of three observations in the eight-day
 193 window was required to accurately model the signal. The closest RTLS parameters in time were
 194 used to normalize the daily data. The normalized Bidirectional Reflectance Factor ($BRFn$) for the
 195 NAD surface reflectance (SZA = 45°, VZA = 0°, RAA = 0°) was calculated using Eq. 1 (Lyapustin
 196 et al., 2018):

197
$$BRFn = BRF \times \frac{k^L + F_{0V} \times k^V + F_{0G} \times k^G}{k^L + F_V \times k^V + F_G \times k^G} \quad (1)$$

198 where k^L , k^V , and k^G are the BRDF isotropic, volumetric, and geometric-optical kernel weights,
 199 respectively; F_{0V} and F_{0G} are the BRDF kernel values for the given geometry listed in Table 2;
 200 and F_V and F_G are the kernel values of the RTLS model for the specific MODIS observation,
 201 respectively (Lyapustin et al., 2018). F_V and F_G values are available at 5-km cells and were
 202 resampled to 1-km using the nearest neighbors' method to match the spatial resolution of the
 203 spectral bands. This resampling step does not create spatial artifacts in the data because the
 204 geometry changes slowly over time (Lyapustin et al., 2018).

205 Table 2 – View-angle normalizations and corresponding BRDF kernel values.

View-angle	Solar Zenith Angle (SZA, °)	View Zenith Angle (VZA, °)	Relative Azimuth Angle (RAA, °)	F_{0V}	F_{0G}
Nadir	45	0	0	-0.04578	-1.10003
Backward scattering	45	35	180	0.22930469	0.017440045
Forward scattering	45	35	0	-0.12029795	-1.6218740

206

207 We aggregated normalized daily data into monthly composites by keeping the median values for
 208 each pixel. During the temporal aggregation, we also calculated the per-pixel number of samples
 209 (or observations) for each monthly composite, which can be used as auxiliary data to filter pixels
 210 with low number of observations (less reliable estimates of surface reflectance). The tiles were
 211 mosaicked for the entire South America and then re-projected from the original sinusoidal
 212 projection to the geographic coordinates system (datum WGS-84, EPSG 4326). The output spatial
 213 resolution corresponded to 0.0091 degrees, which is approximately equivalent to 1 km in
 214 projected coordinates.

215 We also calculated two traditional vegetation indices: NDVI (Rouse et al., 1973) (Eq. 2) and EVI
 216 (Huete et al., 2002) (Eq. 3).

217
$$NDVI = \frac{\rho_{NIR} - \rho_{Red}}{\rho_{NIR} + \rho_{Red}} \quad (2)$$

218
$$EVI = 2.5 \times \frac{\rho_{NIR} - \rho_{Red}}{\rho_{NIR} + (6 \times \rho_{Red} - 7.5 \times \rho_{Blue}) + 1} \quad (3)$$

219 where ρ is the surface reflectance of a MODIS band, ρ_{NIR} is the NIR reflectance (band 2), ρ_{Red}
220 is the red reflectance (band 1), and ρ_{Blue} is the blue reflectance (band 3). The constants in Eq. 3
221 (6, 7.5, 1, and 2.5) represent: the aerosol coefficient adjustment of the atmosphere for the red and
222 blue bands; the adjustment factor for the soil; and the gain factor, respectively (Huete et al., 2002).

223

224 **2.2.2. The anisotropy (ANI) data**

225 For the ANI data, the daily surface reflectance data was first normalized to two viewing-angles at
226 the backward (SZA = 45°, VZA = 35°, RAA = 180°) and forward (SZA = 45°, VZA = 35°, RAA
227 = 0°) scattering using Eq. 1 and values from Table 2. The VZA was set to near hotspot (VZA =
228 35°) instead of the actual hotspot (VZA = 45°) to keep VZA closer to the actual range of MODIS
229 observations across the South America and minimize errors coming from extrapolation of the
230 BRDF (Moura et al., 2015). The standard deviation for this modelling was thoroughly
231 investigated in a previous study and determined as 10% of the observed variation in anisotropy
232 (Moura et al., 2015). Further, we aggregated the backward and forward scattering data temporally
233 into monthly composites following the same procedures as before for the NAD data. We then
234 calculated the NDVI and EVI for each of the view-angle normalizations. Finally, we obtained the
235 difference between backward and forward scattering estimates for each of the eight MODIS
236 bands, as well as for the NDVI and EVI, effectively generating the ANI layers (Eq. 4; Moura et
237 al., 2015):

238
$$ANI_i = Backward_i - Forward_i \quad (4)$$

239 where i is the spectral band or VI selected in the calculation.

240

241 **2.3. Algorithm and computation**

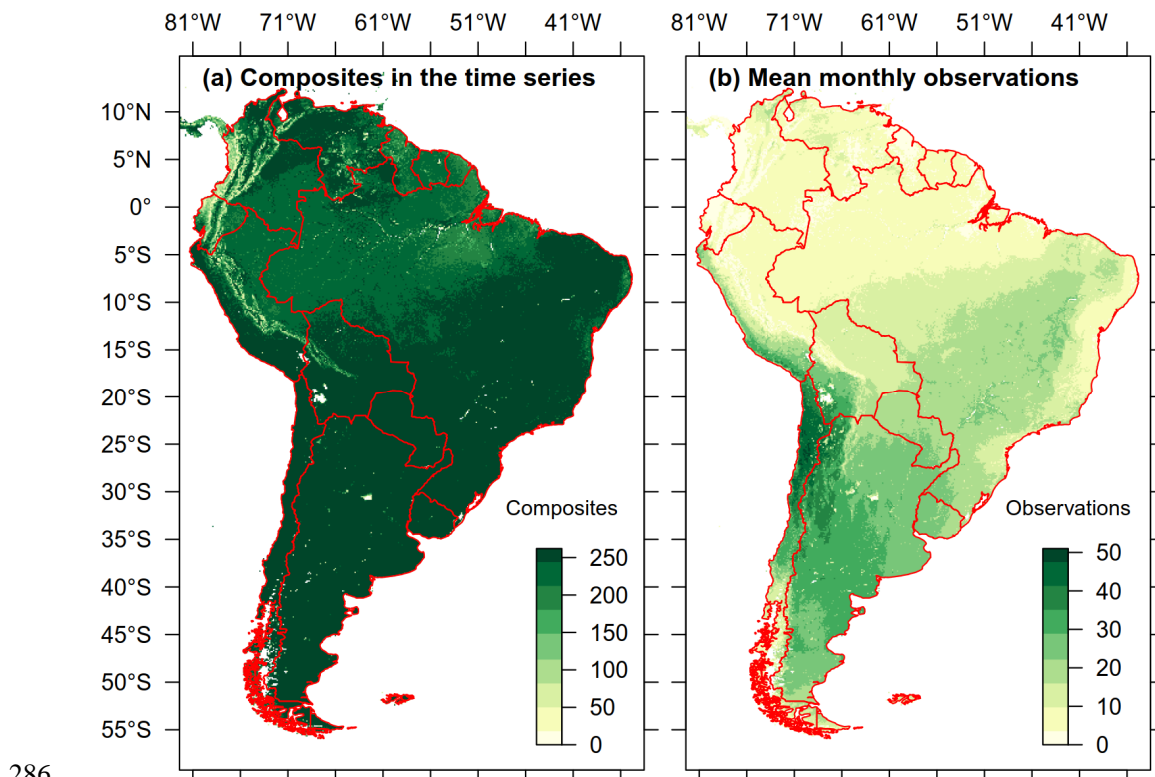
242 All data processing was done in R v4.0.2 (R Core Team, 2016) and the code is available at GitHub
243 (https://github.com/ricds/maiac_processing) (Dalagnol & Wagner, 2022). Besides processing the
244 AnisoVeg product from the daily MAIAC MODIS data, the code can also generate 16-day or 8-
245 day temporal composites, mosaics, and VIs. Although we focused on South America when
246 developing AnisoVeg, the code can readily be adapted to process data for other parts of the world
247 and generate corresponding NAD and ANI layers. Below, we provide the computer specification
248 for anyone who wishes to process the data independently.

249 For the presented dataset, the computation was performed under a HP Z840 Workstation with
250 Intel Xeon CPU E5-2640 v3 (2.60Ghz, 32 cores), and 64 GB (gigabytes) RAM memory. The
251 daily MODIS data for the whole South America from 2000 to 2021 accounted for 6.69 TB
252 (terabytes). Processing monthly composites is computationally intensive due to loading all daily
253 data for each month at once for a given tile. Thus, the main bottlenecks are RAM memory and
254 hard drive writing speed. For the workstation with 64 GB memory, the usage of 10 cores running
255 in parallel processing was the optimal choice. The average processing time of each monthly
256 composite for one tile was 6 minutes. Therefore, it took 26.2 hours to process the 262 composites
257 (March 2000 to December 2021) for each tile. Since we had 31 tiles covering the South America,
258 the total amount of time to process one view-normalization was approximately a month (33.8
259 days). Consequently, the total time spent in computation was 101.5 days for processing the three
260 view-normalizations (nadir, backward, and forward scattering) and generating the NAD and ANI
261 layers. Processing can also be done with less potent computers with a minimum of 16 GB RAM
262 memory and 4 processing cores.

263

264 **2.4. Time series availability and uncertainty**

265 The monthly compositing process returned a time series dataset over all of South America with
 266 an average of 242 ± 35 out of a maximum of 262 composites (period between March 2000 and
 267 December 2021) for each pixel with some data missing due to lack of high-quality observations
 268 (Figure 2). Only 34.3% of the available pixels have the full time series (262 composites). The
 269 Amazon region shows a lower mean number of samples in the time series with an average of 231 ± 29
 270 composites, which can be seen in Figure 2. This lower number of samples is due to the innate
 271 high cloud cover (Durieux et al., 2003). It is important to note that the AnisoVeg product was
 272 strictly created to analyze land surface and does not cover water bodies. Moreover, the period
 273 between March 2000 and June 2002 has higher amounts of missing data because it preceded the
 274 launch of the Aqua satellite. When data from both satellites (Terra and Aqua) were combined to
 275 create the product after 2002, we had a much better pixel level data availability to produce dense
 276 time series. Although we have a dense time series across the Amazon rainforests (Figure 2a), the
 277 mean number of daily observations within a month for this region is relatively lower than that
 278 observed in more dry and seasonal regions of South America (Figure 2b). Thus, we suggest using
 279 the number of samples layer as a proxy for uncertainty on the retrieval of monthly composites to
 280 filter out pixels with low number of samples (e.g., less than three observations per composite).
 281 The lesser number of samples one pixel has, the higher the uncertainty in the data analysis.
 282 Although we use the median values to aggregate observations within months and mitigate
 283 potential land cover changes, stand-replacing changes may cause inaccurate anisotropy estimates
 284 for the given monthly estimates. Hence, we advise filtering data for land use and land cover
 285 changes before using them to obtain the most accurate anisotropy estimates.



286
 287 Figure 2 – AnisoVeg time series availability and uncertainty over South America. (a) The number
 288 of composites in the time series representing pixel availability. The maximum number of
 289 composites in the time series is 262 for the period between March 2000 and December 2021. (b)
 290 Mean number of daily observations within a month used to create the monthly composites as a

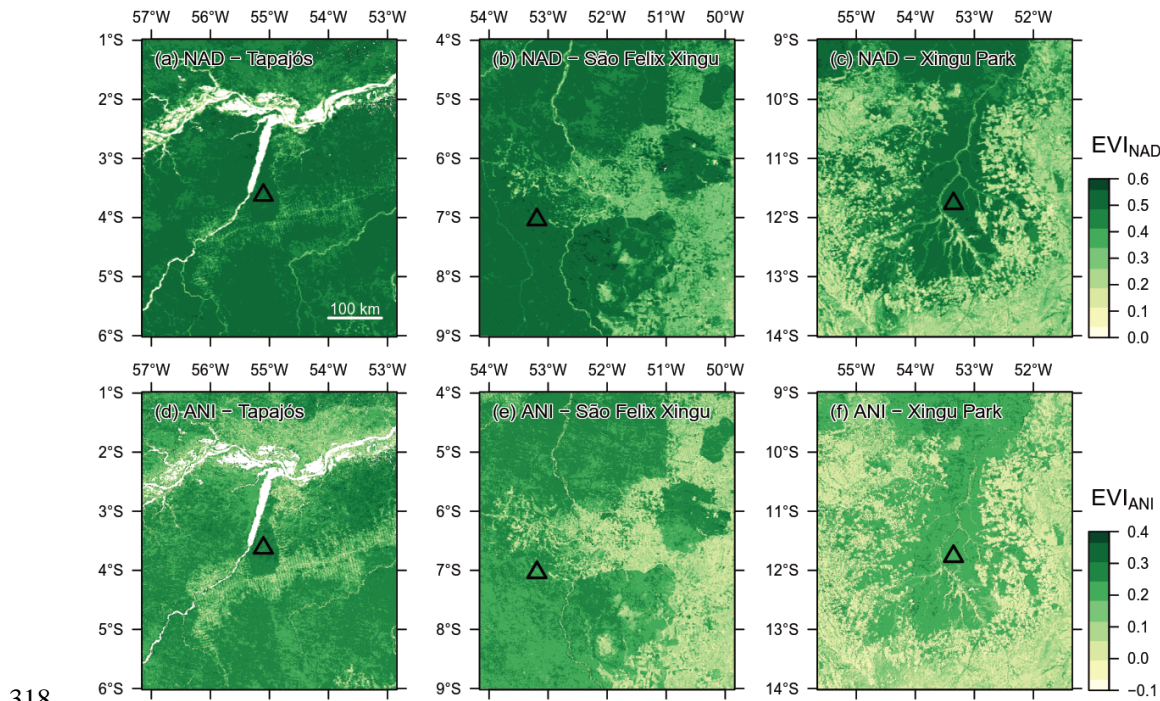
291 proxy for uncertainty. The maximum daily observations in a composite are 60 (twice a day every
292 day for a month).

293

294 **3. Spatial and temporal distribution of NAD and ANI data across the Amazon forests**

295 We selected three experimental areas at the Brazilian Amazon rainforests to show the spatial and
296 temporal distribution of NAD and ANI data (rectangles in Figure 1). These areas show old-growth
297 rainforests with distinct canopy structure and aboveground biomass (AGB) stocks. The AGB
298 increases from semideciduous forests at the Xingu Park ($190 \pm 19 \text{ Mg ha}^{-1}$) and open
299 ombrophilous forests with lianas at the São Felix do Xingu ($241 \pm 31 \text{ Mg ha}^{-1}$) to dense
300 ombrophilous forests at the Tapajós National Forest ($288 \pm 38 \text{ Mg ha}^{-1}$), as estimated by the
301 ESA/CCI AGB map from 2017 (Santoro & Cartus, 2021). These are large-scale AGB estimates
302 and may underestimate the true AGB at higher values such as in the Tapajós site. These three
303 sites are also expected to show different phenological dynamics because their selected pixels
304 cover distinct phenoregions in the study reported by Xu et al. (2015).

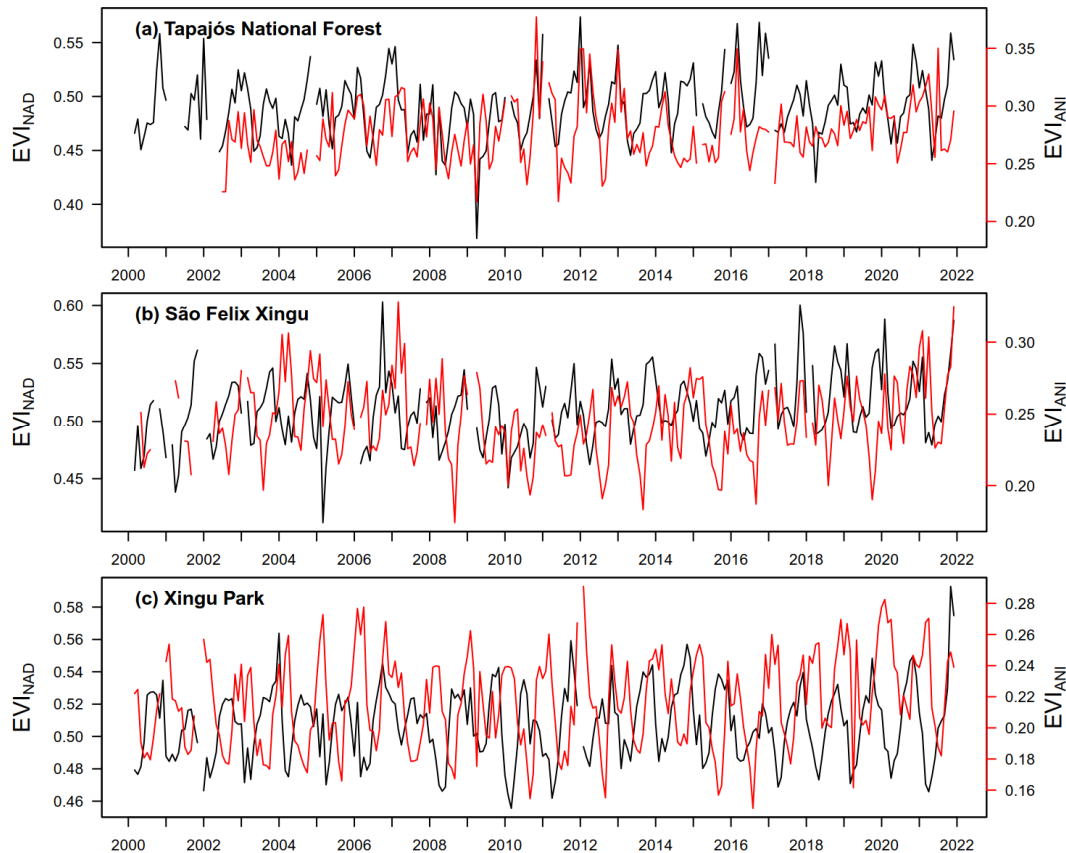
305 When compared to the nadir-normalized EVI (EVI_{NAD}) images (Figures 3a, b, c), the anisotropy
306 EVI (EVI_{ANI}) data showed different spatial patterns across sites (Figures 3d, e, f). While the
307 forests over the three sites showed approximately similar EVI_{NAD} values (EVI_{NAD} ≈ 0.50) (Figures
308 3a,b,c), they showed more variability in EVI_{ANI} between the Xingu Park (EVI_{ANI} > 0.20), São
309 Felix do Xingu (EVI_{ANI} > 0.24), and Tapajós (EVI_{ANI} > 0.27) sites (Figures 3d,e,f). This increase
310 in EVI_{ANI} between sites goes into the same direction of the AGB gradient observed from the
311 Xingu Park to the Tapajós National Forest. This result may indicate different forest canopy
312 structures that were not captured in the EVI_{NAD} observations, but were captured by the EVI_{ANI}.
313 Overall, the EVI_{ANI} is high over forests (0.20 to 0.30) and low over pastures and crops (less than
314 0.10). This means large anisotropy between the reflected energy in backward and forward
315 scattering MODIS directions due to the structural complexity of forest canopies. The association
316 between anisotropy and forest canopy structure has been previously shown for the same region in
317 a previous work (Moura et al., 2016).



318

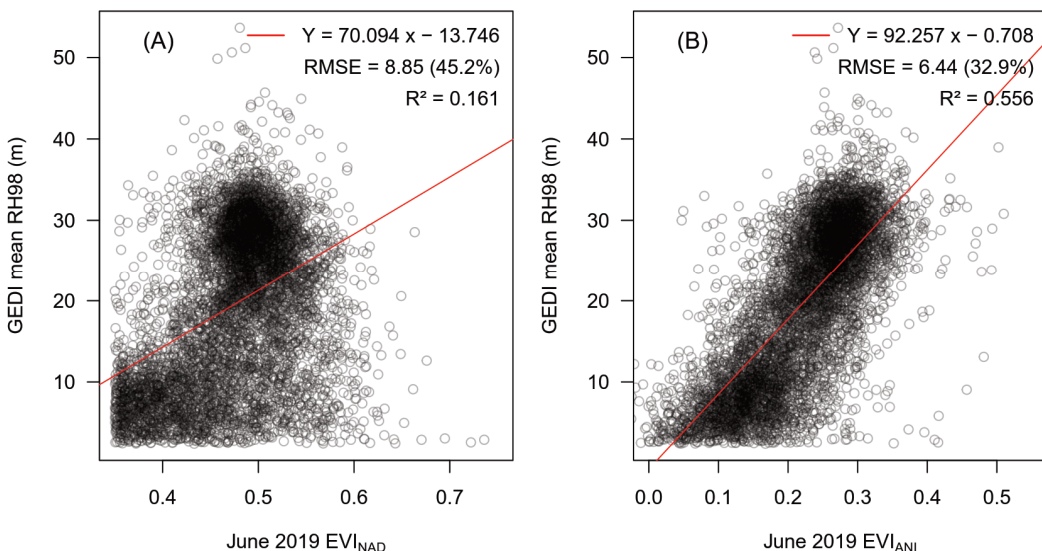
319 Figure 3 – The spatial distribution in August 2020 (dry season) of the nadir-normalized Enhanced
 320 Vegetation Index (EVI_{NAD}) is shown in (a), (b), and (c) for the Tapajós National Forest, São Felix
 321 do Xingu and Xingu Park, respectively. Corresponding results for the anisotropy EVI (EVI_{ANI})
 322 are shown in (d), (e), and (f), respectively. The triangles plotted over (a, b, and c) indicate the
 323 sites used to obtain the profiles of Figure 4.

324 From the comparison of different sites (triangles in Figure 3a), we observed that the mean EVI_{NAD}
 325 signal over the time period did not vary much between the selected forests, while the EVI_{ANI}
 326 varied greatly (Figure 4): Tapajós (mean EVI_{NAD} = 0.49, mean EVI_{ANI} = 0.27), São Felix do Xingu
 327 (mean EVI_{NAD} = 0.51, mean EVI_{ANI} = 0.24), and Xingu Park (mean EVI_{NAD} = 0.51, mean EVI_{ANI}
 328 = 0.22). Moreover, EVI_{NAD} and EVI_{ANI} values were moderately positively correlated at Tapajós
 329 ($r = +0.37$), weakly correlated at São Felix do Xingu ($r = +0.06$), and moderately negatively
 330 correlated at the Xingu Park ($r = -0.28$). The EVI_{NAD} and EVI_{ANI} seasonal variability and phase
 331 correlation changes from site to site, suggesting that different canopy dynamics processes are
 332 likely being captured by the two metrics at the three sites. Understanding exactly what those
 333 effects mean for these forests is beyond the scope of this paper. However, it indicates open venues
 334 for studying forest functioning using these products. For example, previous studies have shown
 335 that EVI_{NAD} metrics captured different compositions of leaf ages in the canopies of the central
 336 Amazon (Gonçalves et al., 2020).



337
 338 Figure 4 – Time series of AnisoVeg's MODIS Enhanced Vegetation Index (EVI) from 2000 to
 339 2021 for old-growth forests of the (a) Tapajós National Forest; (b) São Felix do Xingu;
 340 (c) Xingu Park. The black line indicates the nadir-normalized signal (NAD layer), while the red line
 341 represents the EVI anisotropy (ANI layer). The profiles are the mean value of 3 x 3 pixels whose
 342 locations are indicated by triangles in Figure 3.

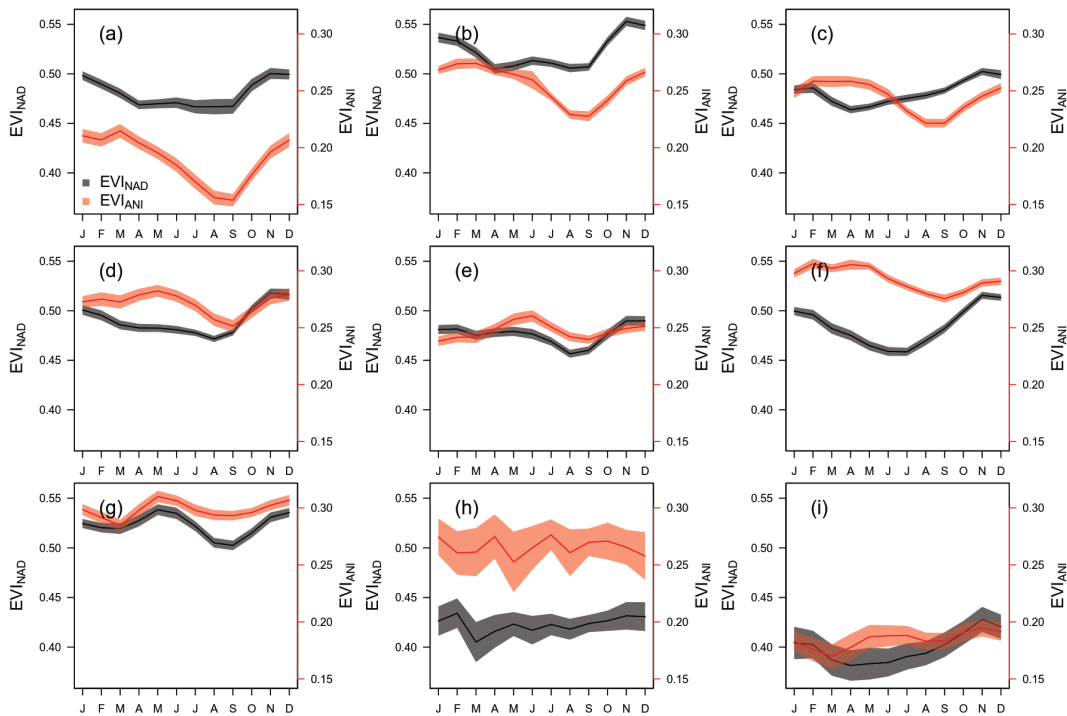
To demonstrate the potential of AnisoVeg for large-scale forest structure inference, we compared the NAD and ANI data against forest height measurements from the Global Ecosystem Dynamics Investigation (GEDI) LiDAR sensor. We found that EVI_{ANI} was able to explain up to 55% of height variability of Amazon forests according to a simple linear relationship ($R^2 = 0.55, p < 0.01$, Figure 5). This is a very strong predicting power for a single variable, considering a simple linear model, especially for satellite passive optical data which are often underrated for forest structure estimates in comparison to Synthetic Aperture Radar (SAR) data. EVI_{NAD} was significantly but weakly associated to height variability ($R^2 = 0.16, p < 0.01$), reinforcing the increase in explanation power owed to the anisotropy metrics built from multi-angle observations. The height data was derived from the GEDI LiDAR sensor aboard the International Space Station. They were obtained more specifically from the product GEDI L2A elevation and height metrics data version 2 (footprint size 25 m), acquired from April 2019 to October 2020 (available dates at the time of download). GEDI data were downloaded from Earth Data cloud service system (<https://earthdata.nasa.gov>). We selected the Relative Height metric at 98th percentile (RH98), which represents the top canopy height. The selected RH98 metric was averaged over each 1-km grid cell, and filtered using a threshold of greater than or equal to 50 shots per km^2 to have a high confidence of reliable height estimation representing the 1-km mean. The AnisoVeg data used for this comparison were based on the same time period as GEDI, and filtered for EVI_{NAD} larger than 0.35 to exclude non-forested areas. While we only showed the plot for the strongest $\text{EVI}_{\text{ANI}}:\text{GEDI}$ relationship in June 2019 (Figure 5), the other months also showed significant ($p < 0.01$) and strong relationships with R^2 ranging from 0.36 to 0.55 (mean $R^2 = 0.46$). Future studies should explore relationships using ANI from different months and other indices, alone or in combination with each other, to further understand their significance for explaining forest structure. This is important to determine how the anisotropy data can contribute for aboveground biomass and carbon estimates in conjunction with other sources of data such as those from SAR sensors.



370 obtained in June 2019 over the Amazon: (a) EVI_{NAD} and (b) EVI_{ANI}. The RH98 metric is the
 371 relative height at the 98th percentile, which represents the top of canopy height. 7,000 random
 372 matching pixels were used in this analysis (1% of 700,000 total matching pixels available),
 373 resulting from the filtering of both GEDI and AnisoVeg data. The red line indicates the fitted line
 374 by a simple linear model.

375 Terrain illumination is a factor of spectral variability, which can affect EVI_{NAD} determination and
 376 its relationship with biophysical attributes of vegetation, as shown by previous literature (Huang
 377 et al., 2010; Chen and Cao, 2012). Even at 1-km spatial resolution, EVI_{ANI} results of Figures 3, 4
 378 and 5 can be affected to some extent by terrain illumination effects observed locally at some sites.
 379 For instance, topographic effects on EVI_{ANI} occurred probably at the São Felix do Xingu site
 380 where topographic roughness, observed in SRTM data (results not shown), was coincident with
 381 increased EVI_{ANI} values in Figure 3E. Furthermore, even in relatively flat terrains, variations in
 382 topographic aspect (surface orientation to Sun) can affect the EVI variability in MODIS data
 383 because of the different amounts of energy reflected in the NIR towards the sensor by inclined
 384 surfaces in the forward and backscattering view directions. Such effects have been observed in
 385 southern Brazil with MODIS at 250-m spatial resolution and increased in magnitude at higher
 386 spatial resolution data obtained by other sensors (Galvão et al., 2016). Therefore, it may prove
 387 useful to include topographic variables in modelling exercises to offset these effects.

388 In a prospective analysis, we also explored the behavior of the two EVI AnisoVeg metrics over
 389 the Amazonian phenoregions mapped by Xu et al. (2015). The EVI_{NAD} and EVI_{ANI} monthly means
 390 over different phenoregions highlighted the strong heterogeneity of the Amazonian forests
 391 (Figure 6). For instance, the profiles showed strong differences between both metrics from
 392 January to September in a phenoregion with well-defined dry and wet seasons (phenoregion one
 393 in Figure 6a at the Xingu Park). Large differences between EVI_{NAD} and EVI_{ANI} were also observed
 394 in some phenoregions without a very long dry season in the northwest Amazon (phenoregion five
 395 in Figure 6e). On the other hand, EVI_{NAD} and EVI_{ANI} showed temporal decoupling in phenoregion
 396 three located at central-east Amazon (Figure 6c). Overall, while the seasonality of EVI_{NAD} has
 397 been investigated by many studies in the past, the seasonality of EVI_{ANI} is something to be further
 398 explored with the support of auxiliary data (e.g., airborne LiDAR and field campaigns). This is
 399 important to better understand the differences in seasonal patterns between both AnisoVeg
 400 metrics.



401
 402 Figure 6 – Monthly means of EVI_{NAD} (black) and EVI_{ANI} (red) for nine phenoregions mapped by
 403 Xu et al. (2015) in the Amazon. The phenoregions are shown in increasing order from 1 to 9 in

404 corresponding panels (a) to (i). They represent forests with similar seasonality and landscape
405 structure. Solid line and shaded area represent the mean and 95% confidence interval around the
406 mean. The values were extracted from 20 years of data (from 2001 to 2021) for 100 random
407 coordinates within each region, and extracted from 3 x 3 windows of pixels.

408

409 **4. Prospective use of the dataset**

410 The NAD layers from the AnisoVeg product have been used in previous studies to explore: the
411 climate drivers of the Amazon forest greening (Wagner et al., 2017); the large-scale Amazon
412 forest sensitivity to drought (Anderson et al., 2018); the structure and dominance of bamboo
413 species in southwest Amazon (Dalagnol et al., 2018); the productivity in a flooded forest in
414 eastern Amazon (Fonseca et al., 2019); the productivity and relationship with Sun-Induced
415 Fluorescence over the Brazilian Caatinga biome (Bontempo et al., 2020); the relationships with
416 leaf-age demography in central Amazon (Gonçalves et al., 2020); and the relationships with fire
417 disturbance and SAR-based Vegetation Optical Depth in southern Amazon (Zhang et al., 2021).

418 The ANI layers from the AnisoVeg product have been mainly used to characterize Amazon forest
419 structure properties (Moura et al., 2015; 2016). These layers now open new venues of
420 investigation on vegetation, including (but not limited to): the characterization of biophysical
421 attributes of forests, including their seasonality and trends; the assessment of changes in
422 vegetation structure due to natural disturbances or degradation (logging, fire, edge effects); and
423 the evaluation of forest health and productivity (greenness and browning). We expect that this
424 dataset contributes to upscaling studies over large areas of key forest properties such as the AGB
425 and canopy roughness (Foody & Curran, 1994; Saatchi et al., 2008). This information is required
426 for dynamic vegetation models to accurately represent the carbon cycle. This dataset is not limited
427 to study Amazonian forests and can be used to explore other biomes of South America such as
428 the Atlantic Forest, savannas (Cerrado), Caatinga, Chaco, Pantanal, and Pampas. Such studies
429 could improve our understanding of large-scale vegetation functioning, carbon storage, and
430 cycling. Ultimately, they can contribute to refine global ecosystem models, and to obtain accurate
431 estimates of carbon cycle in response to climate and environmental change. Furthermore,
432 auxiliary backward and forward scattering data are also available with the dataset. Beyond the
433 use of the provided ANI layers, this effectively allows the computation of several other multi-
434 angular anisotropy indices from the literature (Table 3). The advantage or disadvantage of one
435 specific anisotropy index rather than others is not established in the literature given the range of
436 vegetation applications and the lack of available datasets up to date. We calculated and provided
437 only ANI due to its demonstrated relationships with Amazonian forests structure and functioning
438 (Moura et al., 2015; Moura et al., 2016; Hilker et al., 2017). However, we expect other indices,
439 including ratios and normalized differences between the backward and forward scattering
440 components, offer additional possibilities for tropical vegetation studies which should be explored
441 in future studies.

442

443 Table 3 – Examples of other multi-angular anisotropy indices that can be further calculated using
444 layers of the AnisoVeg product. Lambda represents the selected spectral band or vegetation index.
445 N, B, and F represent nadir-view normalization, backward scattering, and forward scattering
446 estimates, respectively.

Anisotropy Indices	Formula	Reference
Anisotropy index (ANIX)	$\frac{\lambda_B}{\lambda_F}$	Sandmeier et al. (1998)

Nadir BRDF-adjusted NDVI (NDVI_{Iso})	$\frac{NIR_N - RED_N}{NIR_N + RED_N}$	Schaaf et al. (2002)
Hot-spot dark-spot index (HDS_{RED})	$\frac{RED_B - RED_F}{RED_F}$	Lacaze et al. (2002)
Normalized difference between hot-spot and dark-spot index (NDHD_{NIR})	$\frac{NIR_B - NIR_F}{NIR_B + NIR_F}$	Chen et al. (2005)
Hot-spot dark-spot NDVI (NDVI_{HD})	$\frac{NIR_B - RED_F}{NIR_B + RED_F}$	Pocewicz et al. (2007)
Hot-spot-incorporated NDVI (NDVI_{HS})	$NDVI_N \times (1 - RED_B)$	Pocewicz et al. (2007)
Anisotropy difference (ANI)*	$\lambda_B - \lambda_F$	Moura et al. (2015)
Vegetation Structure Index (VSI)	$\frac{NDVI_F - NDVI_B}{1 - NIR_F}$	Sharma et al. (2021)

*ANI is included in the AnisoVeg product. Source: Adapted from Sharma et al. (2021).

447

448

449 5. Code and data availability

450 All code is available at GitHub (https://github.com/ricds/maiac_processing) (Dalagnol &
 451 Wagner, 2022). The full dataset can be found at the official AnisoVeg repository at Zenodo
 452 (<https://doi.org/10.5281/zenodo.3878879>) (Dalagnol et al., 2022). The dataset was organized in
 453 compressed files (“.zip” format) sub-divided by years (currently 2000-2021) and layers (bands 1-
 454 8, NDVI, and EVI) for both nadir-normalization (code = NAD) and anisotropy (code = ANI). The
 455 number of samples layers (code = NO_SAMPLES) are also provided. Inside each compressed
 456 file there will be 12 image files (“.tif” format), one per month, except for the year 2000 which
 457 starts in March. The storage size for the whole dataset is 162.6 GB. The data have a scale factor
 458 of 10,000 to reduce file storage size. Thus, to obtain surface reflectance values of bands or correct
 459 range of values for indices, you should divide the layers by 10,000. The exception is the number
 460 of samples, which already shows the correct range of values from 0 to 60 observations. The dataset
 461 is planned to be updated on a yearly-basis. Auxiliary data that allow the calculation of other
 462 anisotropy metrics (listed in Table 3) are included in two separate Zenodo repositories for
 463 backward (<https://doi.org/10.5281/zenodo.6040300>) (Dalagnol, 2022a) and forward scattering
 464 (<https://doi.org/10.5281/10.5281/zenodo.6048785>) (Dalagnol, 2022b), including the selected
 465 layers Red, NIR, NDVI and EVI. The EVI_{ANI} and EVI_{NAD} layers were also uploaded to the GEE
 466 platform using the *geeup* tool v0.5.3 (Roy, 2022). They can be accessed through the GEE
 467 ImageCollection assets “projects/anisoveg/assets/evi_anisotropy” and
 468 “projects/anisoveg/assets/evi_nadir”, found at
 469 <https://code.earthengine.google.com/?asset=projects/anisoveg/assets/evi_anisotropy> and
 470 <https://code.earthengine.google.com/?asset=projects/anisoveg/assets/evi_nadir>.

471

472 Author contribution

473 R.D. and Y.M. conceived the presented idea. R.D. designed the methodology with contributions
 474 from Y.M. on the anisotropy method. R.D. conducted formal analysis and investigation with
 475 contributions from L.G., F.W., N.G., and S.S. Y.W. and A.L. provided the original MODIS
 476 (MAIAC) data and support for processing it. Y.Y. and S.S. provided the processed GEDI height
 477 data and support to analyze it. R.D. and F.W. developed the code to process the MODIS (MAIAC)
 478 data into the products. R.D. conducted data curation of the products. L.A. supervised the project.
 479 R.D. wrote the original draft with support from L.G., F.W. and Y.M. All authors read, reviewed
 480 and approved the final version of the manuscript.

481

482 **Acknowledgements**

483 R.D. was supported by Sao Paulo Research Foundation (FAPESP) grants 2015/22987-7 and
484 2019/21662-8. F.W. was supported by FAPESP grant 2015/50484-0. Part of this work was carried
485 out at the Jet Propulsion Laboratory, California Institute of Technology, under a contract with the
486 National Aeronautics and Space Administration (NASA). The funders had no role in the study
487 design, data collection and analysis, including the decision to publish or prepare the manuscript.
488 We thank the MODIS MAIAC team from NASA for providing the freely available MODIS
489 (MAIAC) daily dataset. The authors thank the comments from Bruce Nelson and three
490 anonymous reviewers who helped improve this manuscript.

491

492 **Conflict of Interest**

493 The authors have declared no conflict of interest.

494

495 **References**

496 Anderson, L. O., Ribeiro Neto, G., Cunha, A. P., Fonseca, M. G., Mendes de Moura, Y.,
497 Dalagnol, R., Wagner, F. H., & Aragão, L. (2018). Vulnerability of Amazonian forests to
498 repeated droughts. *Philosophical Transactions of the Royal Society B: Biological Sciences*,
499 373(1760), 20170411. <https://doi.org/10.1098/rstb.2017.0411>

500 Bhandari, S., Phinn, S., & Gill, T. (2011). Assessing viewing and illumination geometry effects
501 on the MODIS vegetation index (MOD13Q1) time series: implications for monitoring
502 phenology and disturbances in forest communities in Queensland, Australia. *International
503 Journal of Remote Sensing*, 32(22), 7513–7538.
504 <https://doi.org/10.1080/01431161.2010.524675>

505 Bi, J., Knyazikhin, Y., Choi, S., Park, T., Barichivich, J., Ciais, P., Fu, R., Ganguly, S., Hall, F.,
506 Hilker, T., Huete, A., Jones, M., Kimball, J., Lyapustin, A. I., Mottus, M., Nemani, R. R.,
507 Piao, S., Poulter, B., Saleska, S. R., ... Myneni, R. B. (2015). Sunlight mediated
508 seasonality in canopy structure and photosynthetic activity of Amazonian rainforests.
509 *Environmental Research Letters*, 10(6). <https://doi.org/10.1088/1748-9326/10/6/064014>

510 Bontempo, E., Dalagnol, R., Ponzoni, F., & Valeriano, D. (2020). Adjustments to sif aid the
511 interpretation of drought responses at the caatinga of Northeast Brazil. *Remote Sensing*,
512 12(19), 1–29. <https://doi.org/10.3390/rs12193264>

513 Chen, J. M., Menges, C. H., & Leblanc, S. G. (2005). Global mapping of foliage clumping
514 index using multi-angular satellite data. *Remote Sensing of Environment*, 97(4), 447–457.
515 <https://doi.org/10.1016/j.rse.2005.05.003>

516 Chen, J. M., Liu, J., Leblanc, S. G., Lacaze, R., & Roujean, J. L. (2003). Multi-angular optical
517 remote sensing for assessing vegetation structure and carbon absorption. *Remote Sensing
518 of Environment*, 84(4), 516–525. [https://doi.org/10.1016/S0034-4257\(02\)00150-5](https://doi.org/10.1016/S0034-4257(02)00150-5)

519 Chen, W., & Cao, C. (2012). Topographic correction-based retrieval of leaf area index in
520 mountain areas. *Journal of Mountain Science*, 9(2), 166–174.
521 <https://doi.org/10.1007/s11629-012-2248-2>

522 Dalagnol, R., Wagner, F. H., Galvão, L. S., Nelson, B. W., & Aragão, L. (2018). Life cycle of
523 bamboo in the southwestern Amazon and its relation to fire events. *Biogeosciences*,
524 15(20), 6087–6104. <https://doi.org/10.5194/bg-15-6087-2018>

525 Dalagnol, Ricardo; Galvão, Lênio Soares; Wagner, Fabien Hubert; Moura, Yhasmin Mendes;
526 Gonçalves, Nathan; Wang, Yujie; Lyapustin, Alexei; Yang, Yan; Saatchi, Sassan; Aragão,
527 Luiz Eduardo Oliveira e Cruz. (2022). "AnisoVeg: Anisotropy and Nadir-normalized
528 MODIS MAIAC datasets for satellite vegetation studies in South America". (Version v1)
529 [Data set]. Zenodo. <https://doi.org/10.5281/zenodo.3878879>

530 Dalagnol, Ricardo. (2022a). Back scattering data of AnisoVeg: Anisotropy and Nadir-
531 normalized MODIS MAIAC datasets for satellite vegetation studies in South America
532 [Data set]. Zenodo. <https://doi.org/10.5281/zenodo.6040300>

533 Dalagnol, Ricardo. (2022b). Forward scattering data of AnisoVeg: Anisotropy and Nadir-
534 normalized MODIS MAIAC datasets for satellite vegetation studies in South America
535 [Data set]. Zenodo. <https://doi.org/10.5281/zenodo.6048785>

536 Dalagnol, R., & Wagner, F. H. (2022). maiac_processing: Script and functions to process daily
537 MODIS MAIAC data to BRDF-corrected 16-day and monthly mosaic composites.
538 (Version 1.0) [Computer software]. Zenodo. <https://doi.org/10.5281/zenodo.6561351>

539 de Moura, Y. M., Hilker, T., Lyapustin, A. I., Galvão, L. S., dos Santos, J. R., Anderson, L. O.,
540 de Sousa, C. H. R., & Arai, E. (2015). Seasonality and drought effects of Amazonian
541 forests observed from multi-angle satellite data. *Remote Sensing of Environment*, 171,
542 278–290. <https://doi.org/10.1016/j.rse.2015.10.015>

543 de Sousa, C. H. R., Hilker, T., Waring, R., de Moura, Y. M., & Lyapustin, A. (2017). Progress
544 in remote sensing of photosynthetic activity over the amazon basin. *Remote Sensing*, 9(1),
545 1–23. <https://doi.org/10.3390/rs9010048>

546 Durieux, L., Toledo Machado, L. A., & Laurent, H. (2003). The impact of deforestation on
547 cloud cover over the Amazon arc of deforestation. *Remote Sensing of Environment*, 86(1),
548 132–140. [https://doi.org/10.1016/S0034-4257\(03\)00095-6](https://doi.org/10.1016/S0034-4257(03)00095-6)

549 Fonseca, L. D. M., Dalagnol, R., Malhi, Y., Rifai, S. W., Costa, G. B., Silva, T. S. F., Da Rocha,
550 H. R., Tavares, I. B., & Borma, L. S. (2019). Phenology and Seasonal Ecosystem
551 Productivity in an Amazonian Floodplain Forest. *Remote Sensing*, 11(13), 1530.
552 <https://doi.org/10.3390/rs11131530>

553 Foody, G. M., & Curran, P. J. (1994). Estimation of Tropical Forest Extent and Regenerative
554 Stage Using Remotely Sensed Data. *Journal of Biogeography*, 21(3), 223.
555 <https://doi.org/10.2307/2845527>

556 Galvão, L. S., Breunig, F. M., Santos, J. R. dos, & Moura, Y. M. de. (2013). View-illumination
557 effects on hyperspectral vegetation indices in the Amazonian tropical forest. *International
558 Journal of Applied Earth Observation and Geoinformation*, 21(1), 291–300.
559 <https://doi.org/10.1016/j.jag.2012.07.005>

560 Galvão, L. S., dos Santos, J. R., Roberts, D. A., Breunig, F. M., Toomey, M., & de Moura, Y.
561 M. (2011). On intra-annual EVI variability in the dry season of tropical forest: A case
562 study with MODIS and hyperspectral data. *Remote Sensing of Environment*, 115(9), 2350–
563 2359. <https://doi.org/10.1016/j.rse.2011.04.035>

564 Gao, F., Schaaf, C. B., Strahler, A. H., Jin, Y., & Li, X. (2003). Detecting vegetation structure
565 using a kernel-based BRDF model. *Remote Sensing of Environment*, 86(2), 198–205.
566 [https://doi.org/10.1016/S0034-4257\(03\)00100-7](https://doi.org/10.1016/S0034-4257(03)00100-7)

567 Galvão, L. S., Breunig, F. M., Teles, T. S., Gaida, W., & Balbinot, R. (2016). Investigation of
568 terrain illumination effects on vegetation indices and VI-derived phenological metrics in
569 subtropical deciduous forests. *GIScience and Remote Sensing*, 53(3), 360–381.
570 <https://doi.org/10.1080/15481603.2015.1134140>

571 Gatti, L. V., Basso, L. S., Miller, J. B., Gloor, M., Gatti Domingues, L., Cassol, H. L. G.,
572 Tejada, G., Aragão, L. E. O. C., Nobre, C., Peters, W., Marani, L., Arai, E., Sanches, A.
573 H., Corrêa, S. M., Anderson, L., Von Randow, C., Correia, C. S. C., Crispim, S. P., &
574 Neves, R. A. L. (2021). Amazonia as a carbon source linked to deforestation and climate
575 change. *Nature*, 595(7867), 388–393. <https://doi.org/10.1038/s41586-021-03629-6>

576 Gonçalves, N. B., Lopes, A. P., Dalagnol, R., Wu, J., Pinho, D. M., & Nelson, B. W. (2020).
577 Both near-surface and satellite remote sensing confirm drought legacy effect on tropical
578 forest leaf phenology after 2015/2016 ENSO drought. *Remote Sensing of Environment*,
579 237(April 2019), 111489. <https://doi.org/10.1016/j.rse.2019.111489>

580 Hilker, T., Galvão, L. S., Aragão, L. E. O. C., de Moura, Y. M., do Amaral, C. H., Lyapustin, A.
581 I., Wu, J., Albert, L. P., Ferreira, M. J., Anderson, L. O., dos Santos, V. A. H. F.,
582 Prohaska, N., Tribuzy, E., Barbosa Ceron, J. V., Saleska, S. R., Wang, Y., de Carvalho
583 Gonçalves, J. F., de Oliveira Junior, R. C., Cardoso Rodrigues, J. V. F., & Garcia, M. N.
584 (2017). Vegetation chlorophyll estimates in the Amazon from multi-angle MODIS
585 observations and canopy reflectance model. *International Journal of Applied Earth
586 Observation and Geoinformation*, 58, 278–287. <https://doi.org/10.1016/j.jag.2017.01.014>

587 Hilker, T., Lyapustin, A. I., Tucker, C. J., Hall, F. G., Myneni, R. B., Wang, Y., Bi, J., De
588 Moura, Y. M., & Sellers, P. J. (2014). Vegetation dynamics and rainfall sensitivity of the
589 Amazon. *Proceedings of the National Academy of Sciences of the United States of
590 America*, 111(45), 16041–16046. <https://doi.org/10.1073/pnas.1404870111>

591 Hilker, T., Lyapustin, A. I., Tucker, C. J., Sellers, P. J., Hall, F. G., & Wang, Y. (2012). Remote
592 sensing of tropical ecosystems: Atmospheric correction and cloud masking matter. *Remote
593 Sensing of Environment*, 127, 370–384. <https://doi.org/10.1016/j.rse.2012.08.035>

594 Huete, A., Didan, K., Miura, T., Rodriguez, E., Gao, X., & Ferreira, L. (2002). Overview of
595 the radiometric and biophysical performance of the MODIS vegetation indices. *Remote
596 Sensing of Environment*, 83(1–2), 195–213. [https://doi.org/10.1016/S0034-4257\(02\)00096-2](https://doi.org/10.1016/S0034-4257(02)00096-2)

598 Lacaze, R., Chen, J. M., Roujean, J. L., & Leblanc, S. G. (2002). Retrieval of vegetation
599 clumping index using hot spot signatures measured by POLDER instrument. *Remote
600 Sensing of Environment*, 79(1), 84–95. [https://doi.org/10.1016/S0034-4257\(01\)00241-3](https://doi.org/10.1016/S0034-4257(01)00241-3)

601 Liesenberg, V., Galvão, L. S., & Ponzoni, F. J. (2007). Variations in reflectance with
602 seasonality and viewing geometry: Implications for classification of Brazilian savanna
603 physiognomies with MISR/Terra data. *Remote Sensing of Environment*, 107(1–2), 276–
604 286. <https://doi.org/10.1016/j.rse.2006.03.018>

605 Lucht, W., & Lewis, P. (2000). Theoretical noise sensitivity of BRDF and albedo retrieval from
606 the EOS-MODIS and MISR sensors with respect to angular sampling. *International
607 Journal of Remote Sensing*, 21(1), 81–98. <https://doi.org/10.1080/014311600211000>

608 Lyapustin, A. I., Wang, Y., Laszlo, I., Hilker, T., G.Hall, F., Sellers, P. J., Tucker, C. J., &
 609 Korkin, S. V. (2012). Multi-angle implementation of atmospheric correction for MODIS
 610 (MAIAC): 3. Atmospheric correction. *Remote Sensing of Environment*, 127, 385–393.
 611 <https://doi.org/10.1016/j.rse.2012.09.002>

612 Lyapustin, A., Martonchik, J., Wang, Y., Laszlo, I., & Korkin, S. (2011). Multiangle
 613 implementation of atmospheric correction (MAIAC): 1. Radiative transfer basis and look-
 614 up tables. *Journal of Geophysical Research Atmospheres*, 116(3).
 615 <https://doi.org/10.1029/2010JD014985>

616 Lyapustin, A., & Wang, Y. (2018). MCD19A1 MODIS/Terra+Aqua Land Surface BRF Daily
 617 L2G Global 500m, 1km and 5km SIN Grid V006 [Data set]. *NASA EOSDIS Land*
 618 *Processes DAAC*. <https://doi.org/10.5067/MODIS/MCD19A1.006>

619 Lyapustin, A., Wang, Y., Korkin, S., & Huang, D. (2018). MODIS Collection 6 MAIAC
 620 algorithm. *Atmospheric Measurement Techniques*, 11(10), 5741–5765.
 621 <https://doi.org/10.5194/amt-11-5741-2018>

622 Lyapustin, A., Zhao, F., & Wang, Y. (2021). A Comparison of Multi-Angle Implementation of
 623 Atmospheric Correction and MOD09 Daily Surface Reflectance Products From MODIS.
 624 *Frontiers in Remote Sensing*, 2(December), 1–15.
 625 <https://doi.org/10.3389/frsen.2021.712093>

626 Matricardi, E. A. T., Skole, D. L., Costa, O. B., Pedlowski, M. A., Samek, J. H., & Miguel, E. P.
 627 (2020). Long-term forest degradation surpasses deforestation in the Brazilian Amazon.
 628 *Science*, 369(6509), 1378–1382. <https://doi.org/10.1126/SCIENCE.ABB3021>

629 Morton, D. C., Nagol, J., Carabajal, C. C., Rosette, J., Palace, M., Cook, B. D., Vermote, E. F.,
 630 Harding, D. J., & North, P. R. J. (2014). Amazon forests maintain consistent canopy
 631 structure and greenness during the dry season. *Nature*, 506(7487), 221–224.
 632 <https://doi.org/10.1038/nature13006>

633 Moura, Y. M. de, Hilker, T., Gonçalves, F. G., Galvão, L. S., dos Santos, J. R., Lyapustin, A.,
 634 Maeda, E. E., & de Jesus Silva, C. V. (2016). Scaling estimates of vegetation structure in
 635 Amazonian tropical forests using multi-angle MODIS observations. *International Journal*
 636 *of Applied Earth Observation and Geoinformation*, 52(January), 580–590.
 637 <https://doi.org/10.1016/j.jag.2016.07.017>

638 Pocewicz, A., Vierling, L. A., Lentile, L. B., & Smith, R. (2007). View angle effects on
 639 relationships between MISR vegetation indices and leaf area index in a recently burned
 640 ponderosa pine forest. *Remote Sensing of Environment*, 107(1–2), 322–333.
 641 <https://doi.org/10.1016/j.rse.2006.06.019>

642 R Core Team. (2016). *R: A Language and Environment for Statistical Computing* (3.3.1; Vol. 1,
 643 Issue C, p. 2016). R Foundation for Statistical Computing. <https://www.r-project.org/>

644 Samapriya Roy. (2022). samapriya/geeup: geeup: Simple CLI for Earth Engine Uploads (0.5.3).
 645 Zenodo. <https://doi.org/10.5281/zenodo.5814026>

646 Rouse, J. W., Hass, R. H., Schell, J. A., & Deering, D. W. (1974). Monitoring Vegetation
 647 Systems in the Great Plains with ERTS. *Third Earth Resources Technology Satellite-1*
 648 *Symposium*, 1, 301–317.

649 Saleska, S. R., Wu, J., Guan, K., Araujo, A. C., Huete, A., Nobre, A. D., & Restrepo-Coupe, N.
650 (2016). Dry-season greening of Amazon forests. *Nature*, 531(7594), E4–E5.
651 <https://doi.org/10.1038/nature16457>

652 Samanta, A., Ganguly, S., Hashimoto, H., Devadiga, S., Vermote, E., Knyazikhin, Y., Nemani,
653 R. R., & Myneni, R. B. (2010). Amazon forests did not green-up during the 2005 drought.
654 *Geophysical Research Letters*, 37(5), 1–5. <https://doi.org/10.1029/2009GL042154>

655 Samanta, A., Knyazikhin, Y., Xu, L., Dickinson, R. E., Fu, R., Costa, M. H., Saatchi, S. S.,
656 Nemani, R. R., & Myneni, R. B. (2012). Seasonal changes in leaf area of Amazon forests
657 from leaf flushing and abscission. *Journal of Geophysical Research: Biogeosciences*,
658 117(1), 1–13. <https://doi.org/10.1029/2011JG001818>

659 Sandmeier, S., Müller, C., Hosgood, B., & Andreoli, G. (1998). Physical mechanisms in
660 hyperspectral BRDF data of grass and watercress. *Remote Sensing of Environment*, 66(2),
661 222–233. [https://doi.org/10.1016/S0034-4257\(98\)00060-1](https://doi.org/10.1016/S0034-4257(98)00060-1)

662 Santoro, M., & Cartus, O. (2021). *ESA Biomass Climate Change Initiative (Biomass_cci): Global datasets of forest above-ground biomass for the years 2010, 2017 and 2018* (No. 2). Centre for Environmental Data Analysis.
663 <https://doi.org/http://dx.doi.org/10.5285/84403d09cef3485883158f4df2989b0c>

664 Schaaf, C. B., Gao, F., Strahler, A. H., Lucht, W., Li, X., Tsang, T., Strugnell, N. C., Zhang, X.,
665 Jin, Y., Muller, J., Lewis, P., Barnsley, M., Hobson, P., Disney, M., Roberts, G.,
666 Dunderdale, M., Doll, C., Robert, P., Hu, B., ... Roy, D. (2002). Schaaf et al 2002 First
667 operational BRDF, albedo nadir reflectance products from MODIS.pdf. *Remote Sensing of
668 Environment*, 83, 135–148.

669 Wagner, F. H., Hérault, B., Rossi, V., Hilker, T., Maeda, E. E., Sanchez, A., Lyapustin, A. I.,
670 Galvão, L. S., Wang, Y., & Aragão, L. E. O. C. (2017). Climate drivers of the Amazon
671 forest greening. *PLoS ONE*, 12(7), 1–15. <https://doi.org/10.1371/journal.pone.0180932>

672 Wanner, W., Li, X., & Strahler, a H. (1995). On the derivation of kernels for kernel-driven
673 models of bidirectional reflectance. *Journal of Geophysical Research*, 100(D10), 21077.
674 <https://doi.org/10.1029/95JD02371>

675 Wei, H., Zhang, L., Furumi, S., Muramatsu, K., Daigo, M., & Li, P. (2010). Topographic effects
676 on estimating net primary productivity of green coniferous forest in complex terrain using
677 Landsat data: A case study of Yoshino Mountain, Japan. *International Journal of Remote
678 Sensing*, 31(11), 2941–2957. <https://doi.org/10.1080/01431160903140829>

679 Wu, J., Kobayashi, H., Stark, S. C., Meng, R., Guan, K., Tran, N. N., Gao, S., Yang, W.,
680 Restrepo-Coupe, N., Miura, T., Oliviera, R. C., Rogers, A., Dye, D. G., Nelson, B. W.,
681 Serbin, S. P., Huete, A. R., & Saleska, S. R. (2018). Biological processes dominate
682 seasonality of remotely sensed canopy greenness in an Amazon evergreen forest. *New
683 Phytologist*, 217(4), 1507–1520. <https://doi.org/10.1111/nph.14939>

684 Xu, L., Saatchi, S. S., Yang, Y., Myneni, R. B., Frankenber, C., Chowdhury, D., & Bi, J.
685 (2015). Satellite observation of tropical forest seasonality: Spatial patterns of carbon
686 exchange in Amazonia. *Environmental Research Letters*, 10(8).
687 <https://doi.org/10.1088/1748-9326/10/8/084005>

690 Zhang, H., Hagan, D. F. T., Dalagnol, R., & Liu, Y. (2021). Forest Canopy Changes in the
691 Southern Amazon during the 2019 Fire Season Based on Passive Microwave and Optical
692 Satellite Observations. *Remote Sensing*, 13(12), 2238. <https://doi.org/10.3390/rs13122238>